Network: Computation in Neural Systems
March 2006; 17: 3–29

Taylor & Francis
Taylor & Francis Group

Dynamics of neural populations: Stability and synchrony

LAWRENCE SIROVICH, AHMET OMURTAG, & KIP LUBLINER

Laboratory of Applied Mathematics, Mount Sinai School of Medicine, 1 Gustave L. Levy Place, New York, NY 10029, USA

(Received 24 February 2005; accepted 19 October 2005)

Abstract
A population formulation of neuronal activity is employed to study an excitatory network of (spiking) neurons receiving external input as well as recurrent feedback. At relatively low levels of feedback, the network exhibits time stationary asynchronous behavior. A stability analysis of this *time stationary* state leads to an analytical criterion for the critical gain at which time asynchronous behavior becomes unstable. At instability the dynamics can undergo a supercritical Hopf bifurcation and the population passes to a synchronous state. Under different conditions it can pass to synchrony through a subcritical Hopf bifurcation. And at high gain a network can reach a *runaway* state, in finite time, after which the network no longer supports bounded solutions.

The introduction of time delayed feedback leads to a rich range of phenomena. For example, for a given external input, increasing gain produces transition from asynchrony, to synchrony, to asynchrony and finally can lead to divergence. Time delay is also shown to strongly mollify the amplitude of synchronous oscillations. Perhaps, of general importance, is the result that synchronous behavior can exist only for a narrow range of time delays, which range is an order of magnitude smaller than periods of oscillation.

Keywords: *Neural populations, multistates, stability, synchronous oscillations*

Introduction

There is widespread theoretical and computational evidence that populations of interconnected *oscillators* exhibit synchronous behavior (Arnold 1965; Peskin 1975; Mirollo & Strogatz 1990; Schuster & Wagner 1990; Abbott & van Vreeswijk 1993; Kuramoto 1991; Tsodyks et al. 1993; Niebur et al. 1991; Strogatz 2003). Of fundamental importance in neuroscience is the fact that various forms of synchronous behavior have been found in laboratory investigations, see Singer and Gray (1995) for a review. It has been suggested that such activity is fundamental to the transmission of pre-cortical and cortical information as well as to the intrinsic rhythm of a neuronal population in performing its function (Sillito et al. 1994; Castelo-Branco et al. 1998). (But see Ghose & Freeman (1997)). In particular, gamma frequency oscillations (20–60 hz), in cortex, have been proposed as being responsible for *binding* the elements that define an object in relation to the rest of the *world* (Milner 1974; Von der Malsberg 1994; Singer & Gray 1995). However, the true purpose of synchronous oscillations in cortex remains an open question, and its consequences are not

Correspondence: Lawrence Sirovich, Laboratory of Applied Mathematics, Center for Biomathematical Sciences, Box 1012, Mount Sinai School of Medicine, 1 Gustave L. Levy Place, New York, NY 10029, USA. Tel: 212-241-3994; Fax: 212-426-5037; E-mail: chico@camelot.mssm.edu

ISSN: 0954-898X print / ISSN 1361-6536 online
DOI: 10.1080/09548980500421154

well understood. As will be seen, synchronous activity occurs under wide circumstances in modeling neuronal populations.

A frequently observed feature of population models is the existence of excessive activity and as will be seen, sometimes divergence. Addressing a related issue, Abeles (1991) has pointed out that cortex maintains a delicate balance between excitation and inhibition. In particular, in cortex, considerable excitation is balanced by just enough inhibition to hold the population in check. One consequence of such a state of affairs might be the ability of the population to dynamically exchange *attractors*, i.e., to rapidly transform to another, perhaps, more desirable state. This suggestion, and the need for it, until more evidence is available, remains speculation.

The role of inhibition in causing synchronous behavior has been studied in some depth by Brunel and Hakim (1999). Inhibition as an enhancing effect was already observed in *Limulus* (Ratliff et al. 1969), and many studies have focused on the role of inhibition in synchrony (Cobb et al. (1995); Lytton & Sejnowski (1991); see review by Ritz & Sejnowski (1997). Using substantially different methods, we study the effect of excitatory feedback. As will be seen, feedback, coupled with delay, produces a rich repertoire of behaviors, having some contact with dynamics produced under inhibition.

We examine these issues, using the novel approach for the treatment of assemblies of interacting neurons, introduced by Knight et al. (1996). Precursors to the treatment may be found in works of Stein (1965), Wilbur and Rinzel (1982), Abbott and van Vreeswijk (1993), Kuramoto (1991) and Gerstner (1995). A general derivation of equations governing population activity, viewed as a kinetic theory, was presented in Omurtag et al. (2000a), and allows for finite jumps in membrane voltage. Excellent agreement was found between large scale direct simulations of interacting neurons, and comparable population studies. Generalizations and variations of the approach have since appeared in the literature (Sirovich et al. 2000; Nykamp & Tranchina 2000; Casti et al. 2002; Haskell et al. 2001; Omurtag et al. 2000b; de Kamps 2003; Cai et al. 2004). A general and wide ranging study by Knight (2000) showed the effectiveness of eigenanalysis in revealing underlying phenomena and mechanisms. Other related studies have been presented (Knight et al. 2000; Mattia & Del Giudice 2002). An eigenanalysis for a simple finite jump population model is given in Sirovich (2003). As will be seen below, an eigenanalysis is also effective in non-linear situations.

After reviewing the existence of equilibria (Sirovich et al. 2000), we consider the stability of equilibria under a wide set of circumstances. Some insight into stability is furnished by a heuristic discussion, and this is followed by a formal, and more complete, linearized analysis, and its ensuing eigentheory. From this, we analytically determine boundaries of stability. The introduction of time delay is found to lead to a rich range of phenomena. In particular, delay can be destabilizing and the population can enter a state of synchrony. Such synchronous behavior is found to be possible only for a narrow range of time delay, a result that may be significant in light of the above introductory remarks.

The issue of stability and synchrony of neuronal populations has recently attracted much interest (Gerstner 1995; Amit & Brunel 1997; Fusi & Mattia 1999; Mattia & Del Giudice 2002; Naundorf et al. 2005), and the subject is well reviewed in Gerstner (2000). In two studies (Amit & Brunel 1997; Fusi & Mattia 1999) there is an indication that two different asynchronous states of a population can coexist under the same conditions. By and large we find that only one stable attractor exists (synchronous or asynchronous) under multistate conditions. In general this solution is found to be the solution of lowest firing rate. Only for the case of large time delay, when synchrony is absent, do we find two and even three stable asynchronous equilibria. Moreover, in these cases the higher firing rate equilibria are found to have relatively small basins of attraction. This possible discrepancy with the cited

work may be due to differences in models, e.g., in Fusi and Mattia (1999) a constant leakage rather than a voltage dependent leakage is assumed, as well as other differences.

Formulation

We consider an assembly of neurons which follow integrate-and-fire dynamics,

$$\frac{dv}{dt} = -\gamma v + s;\ 0 \le v \le 1. \tag{1}$$

Here, v represents the membrane voltage, normalized so that $v = 0$ represents the resting state and $v = 1$ the threshold for firing. When a neuron voltage achieves threshold, $v = 1$, it is reset to its resting state, $v = 0$. In Equation 1, γ, a rate, represents leakage, and s, also a rate, represents the *current* entering the neuron. In the case to be studied, synaptic arrivals at a neuron result in (normalized) voltage *jumps* of size h. (At a more basic level, synaptic arrivals produce conductance changes (Haskell et al. 2001), which if the typically short time scale is ignored, produces a voltage jump.) In the normalized units of Equation 1, the charging current is the product of the charge delivered by each synaptic event times the rate of arrival of those events. The mean synaptic arrival rate is therefore given by

$$\sigma = s/h. \tag{2}$$

It should be mentioned that the treatment to be presented can be extended to include stochastic jump sizes (see Appendix 1), a reset different than the resting state, a neuronal dead-time, finite synaptic times and finite delays (see Appendix 2). Extensions to even more detailed neuronal dynamics are also feasible and have been explored (Nykamp & Tranchina 2000; Haskell et al. 2001; Casti et al. 2002). In choosing a simplified model, we unburden ourselves of a cumbersome formal apparatus while still retaining a meaningful, though relatively minimal, model.

A population of like neurons that dynamically follows Equation 1 can be characterized by

$$\rho = \rho(v, t), \tag{3}$$

the probability that a member of the population is at membrane potential v, at time t. Since ρ is a probability, we must have

$$\int_0^1 \rho(v, t)dv = 1. \tag{4}$$

Under general conditions it has been shown that the evolution of ρ is governed by a kinetic equation (Knight 2000),

$$\frac{\partial \rho}{\partial t} = -\frac{\partial}{\partial v}\mathcal{J}[\rho];\quad 0 \le v \le 1, \tag{5}$$

and for neurons respecting Equation 1,

$$\mathcal{J}[\rho] = -\gamma v\rho + \frac{s}{h}\int_{v-h}^{v} \rho(v', t)dv', \tag{6}$$

(Omurtag et al. 2000a). From Equation 5 $\mathcal{J}$ has the interpretation of being the local flux of neurons across the interval, $(0, 1)$, of interest. The first term of Equation 6 describes advection to the left, due to leakage, and the second, the flux to the right, due to synaptic arrivals. Thus, when Equation 6 is substituted into 5 we obtain

$$\frac{\partial \rho}{\partial t} = \gamma\frac{\partial}{\partial v}(v\rho) + \frac{s}{h}\{\rho(v - h) - \rho(v)\} = L(s)\rho, \tag{7}$$

which underlines the linear form of L. A precursor to Equation 7 can be found in Stein (1965) (Also see Wilbur & Rinzel [1982] and Holden (1976)).

A quantity of importance is

$$r(t) = \mathcal{J}(\mathrm{v} = 1), \tag{8}$$

the rate at which neurons leave the interval, and hence the firing rate (per neuron). For condition 4 to hold, the population must be *renewed* at the origin at the same rate

$$\mathcal{J}(0) = \mathcal{J}(1), \tag{9}$$

a boundary condition for Equation 5. A simple argument indicates that

$$\rho(1) = 0, \tag{10}$$

thus an absorbing boundary at $v = 1$, is a second boundary condition (Omurtag et al. 2000a). As a result, we can write the firing rate, Equation 8, in the form

$$r(t) = \sigma \int_{1-h}^{1} \rho(v', t)dv' = \frac{s}{h} \int_{1-h}^{1} \rho(v', t)dv'. \tag{11}$$

In many instances it is useful to distinguish between the arrival rate, σ (and current, s) due to external sources, which we denote by

$$\sigma^{\mathbf{e}} = \frac{s^{\mathbf{e}}}{h} \tag{12}$$

and the total arrival rate, which we denote by $\sigma_{\mathbf{t}}$. The latter is composed of $\sigma^{\mathbf{e}}$ and the effect of the (average) number of feedback connections, the *gain*, denoted by G. In terms of equivalent currents, we have

$$s_{\mathbf{t}}(t) = s^{\mathbf{e}}(t) + gr(t); \quad g = hG, \tag{13}$$

where $g = hG$ can be regarded as the gain in voltage jump. In the customary parlance, $G = 0$ is said to be the open loop case, and $G \neq 0$, the closed loop case. (In general situations we forgo super and sub-scripts.) Each terminology offers equivalent representations, see Equation 12, and their differing emphasis makes both terminologies useful in the discussion. This is illustrated in Figure 1, which portrays the feedback loop in terms of both currents and equivalent arrival rates, in brackets.

In keeping with a minimal model we do not include inhibition (see Brunel & Hakim (1999)), which in our formulation is appropriately treated by including a separate interacting inhibitory population. If we define the linear functional of ρ

$$k(t) = \int_{1-h}^{1} \rho(w, t)dw = \frac{h}{s} r \tag{14}$$

the kinetic Equation 7, with feedback stated explicitly, takes the form

$$\frac{\partial \rho}{\partial t} = \gamma \frac{\partial}{\partial v}(v\rho) + \frac{s^{\mathbf{e}}}{1 - Gk}\{\rho(v - h) - \rho(v)\}/h. \tag{15}$$

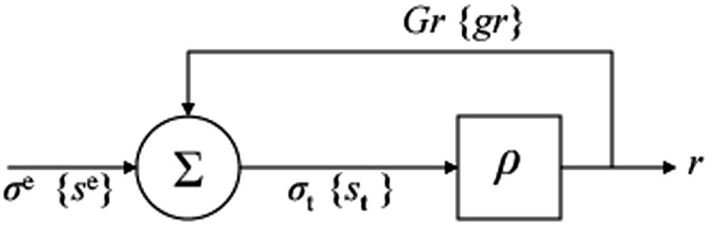

Figure 1. Feedback schematic for Equation 13 indicated in brackets { }. For, the equivalent arrival rate form, $\sigma = s/h$, we get the unbracketed notation.

The denominator which appears in Equation 16 foreshadows the possibility of divergence when G is large, a feature that will be considered later. Thus, ρ is governed by a non-linear integro-differential equation, with a superficial resemblance to the nonlinear Boltzmann equation of kinetic theory (Omurtag et al. 2000a). This basic framework has figured in the various populational studies already cited above.

The derivation of Equation 5, and hence 15, is based on consideration of a population of like neurons that may interact with one another, each neuron following the dynamics dictated by Equation 1. Smooth behavior is achieved by ensemble averaging over suitably replicated systems. In keeping with actual neuron populations, this formulation allows for a synaptic fail rate (Abeles 1991), so that G as in Equation 13 is the average gain. As shown in Omurtag et al. (2000a) the direct simulation of a neuronal population carried out in the fashion specified, produces the same outcome as the kinetic equation, 15.

In interpreting the behavior displayed by Equation 15 one should bear in mind that this is an equation whose derivation includes, in an essential way, the stochasticity of arrivals and connectivity among neurons (Omurtag et al. 2000a). For h small, a formal analysis produces a diffusion equation (Sirovich et al. 2000). However, Equation 15 is a novel operator, which, unlike the diffusion approximation, propagates discontinuities with finite speed, among other distinctions.

Equilibria

Thus far, only the membrane potential, v, and the synaptic jump size, h, have been made dimensionless. Leakage, γ, and the mean rate of synaptic arrivals, σ, still carry a physical dimension, viz., inverse seconds. The ratio of these rates as they appear in Equation 7 is given by

$$\theta = \frac{s}{\gamma h} = \frac{\sigma}{\gamma}. \tag{16}$$

In most circumstances, s/γ is of crucial interest, since it is the ratio of convection to the right, s, to leakage (to the left) at $v = 1$. For example, if in Equation 1 s is a (non-stochastic) constant, then Equation 1 does not lead to neuronal firing if $\gamma > s$. Different dimensionless forms prove useful, and we note that the asymptotic limit $\theta \gg 1$ is equivalently treated by taking $0 < h \ll 1$, with s/γ fixed.

The equilibrium solution, U, of Equation 7 is determined by

$$0 = \gamma \frac{\partial}{\partial v}(vU) + s_{\mathbf{t}} \frac{\{U(v-h) - U(v)\}}{h} + s_{\mathbf{t}} \frac{1}{h} \int_{1-h}^{1} U(v) dv \delta(v), \tag{17}$$

where $s_{\mathbf{t}}$ is the total current, Equation 13, and from the boundary condition 9, the delta function at the origin has been explicitly introduced. An important observation is that the equilibrium solution, which only depends on $s_{\mathbf{t}}$,

$$U = U(v; s_{\mathbf{t}}), \tag{18}$$

encompasses the range of solutions for which $s^{\mathbf{e}}$ and Gh are such that the total current,

$$s_{\mathbf{t}} = s^{\mathbf{e}} + Ghr(s_{\mathbf{t}}), \tag{19}$$

is constant. This determines a locus of external input, $s^{\mathbf{e}}$, and gain, G, for which Equation 18 is the sole equilibrium solution. Otherwise said, a given *open loop* equilibrium solution for which, $s_{\mathbf{t}} = s^{\mathbf{e}}$, furnishes a class of *closed loop* equilibrium solutions given by Equation 19,

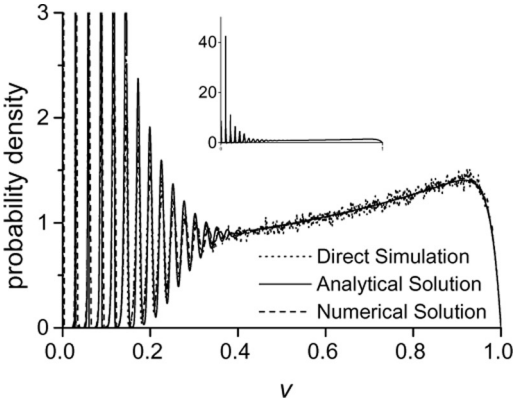

Figure 2. A typical equilibrium solution, calculated for $s/\gamma = 3$. For numerical calculations in this paper: $h = .03$, $\gamma = 20$. Details of the analytical solution are given in Sirovich et al. (2000). The direct simulation is based on a population of 90,000 neurons (Omurtag et al. 2000a). Note the ordinate is truncated, and the full range is indicated by the inset. Up to $v = .2$ are 6 clearly visible voltage jumps, consistent with the given value of h.

see Figure 1. Also noteworthy is the observation that the linear case, Equation 17, generates a range of solutions for the non-linear case 15.

A typical equilibrium solution (Sirovich et al. 2000) is shown in Figure 2. To understand the structure, we note that the renewal of neurons dictated by Equation 9 manifests itself as a delta function in U at the origin, $v = 0$. As Equation 17 expresses, the source of neurons which appear at some location v, lies to the left at $v' = v - h$. Thus, the delta function at the origin produces a discontinuity at $v = h$, with slowly back-drifting neurons at a large population density just to the left of $v = h$. Similar features, which are successively smoothed with diminished maxima occur at integer multiples of h, as is clear in Figure 2. We mention in passing that the *jumping* behavior is lost under the diffusion approximation.

Next the solution undergoes smooth decrementing oscillations and then enters a regime where

$$\rho(v) \propto \frac{1}{s - \gamma v}. \tag{20}$$

Finally, a boundary layer is encountered at $v \approx 1$, since ρ must vanish there. This description embodies the underlying methodology which was used in developing the analytical form of the equilibrium solution (Sirovich et al. 2000).

Heuristic considerations

On a basic level, neuronal response depends on synaptic arrivals. If we denote these stochastic arrival times by $\{t_n\}$ then the *current* which appears in Equation 1 is characterized by

$$s = h \sum_n \delta(t - t_n). \tag{21}$$

The derivation of the population equation, 7, entails a suitable ensemble average (Omurtag et al. 2000a), and σ the synaptic arrival rate which appears in Equation 7 is given by

$$\sigma = \left\langle \sum_n \delta(t - t_n) \right\rangle, \tag{22}$$

where $\langle\rangle$ denotes ensemble average.

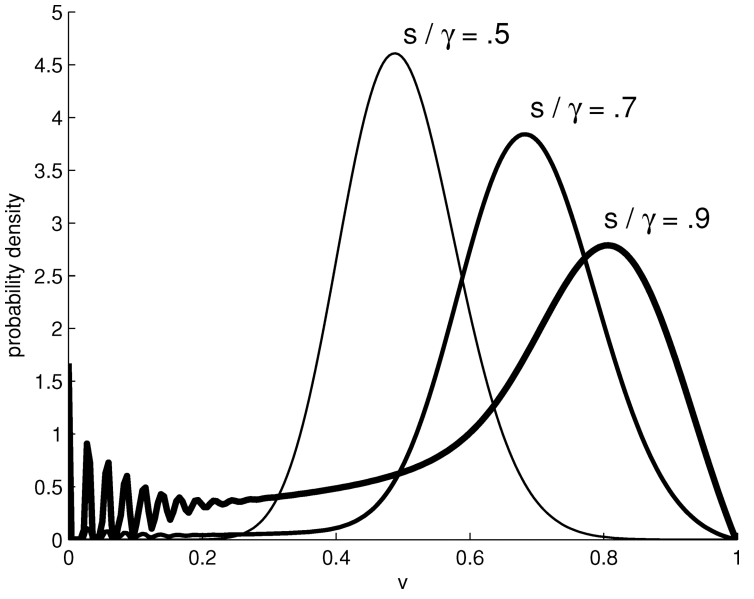

Figure 3. Three equilibria conditions under which Equation 1 would not fire under a non-stochastic and steady current: $s/\gamma = .9$ population firing is apparent; $s/\gamma = .7$ firing is much reduced; $s/\gamma = .5$, an imperceptible firing level.

There is an important distinction between solving Equation 1 with a current given by 21, and with a non-stochastic current of the same average value. As already remarked, for a non-stochastic and constant current, if $s < \gamma$ the neuron does not fire. On the other hand even if Equation 21 obeys $\langle s \rangle < \gamma$, one can easily envision unusual bursts of synaptic arrivals for which a neuron, governed by Equation 1, does fire. This is brought out vividly in the population approach, which includes the effect of stochastic arrivals. Figure 3 shows the equilibrium solution for three cases $s/\gamma = .9, .7, .5$, under which Equation 1 does not fire. Clearly the first case shows evidence of pronounced neuronal firing while the second shows hints of firing. The population firing rate, r, versus constant input current, $s_{\mathbf{t}}$, can be calculated from Equation 11, and is plotted in Figure 4. We see from this that even when the leak, γ, appreciably exceeds the current s, there is a significant range over which the population fires, a clear consequence of stochastic arrivals.

With the explicit form of $r(s_{\mathbf{t}})$, calculated numerically from Equation 11, we can determine the external current $s^{\mathbf{e}}$, which from Equation 19 is given by

$$s^{\mathbf{e}} = s_{\mathbf{t}} - hGr(s_{\mathbf{t}}). \tag{23}$$

From this, it follows that for any G, the construction of Equation 23 is a straightforward geometrical construction, and examples are shown in Figure 5. For fixed G, the differential of 23 yields

$$(1 - hGr'(s_{\mathbf{t}}))ds_{\mathbf{t}} = ds^{\mathbf{e}}, \tag{24}$$

which can be interpreted as giving the amplification $ds_{\mathbf{t}}$ for an increment of excitation, $ds^{\mathbf{e}}$. On the locus

$$hr'(s_{\mathbf{t}})G - 1 = 0, \tag{25}$$

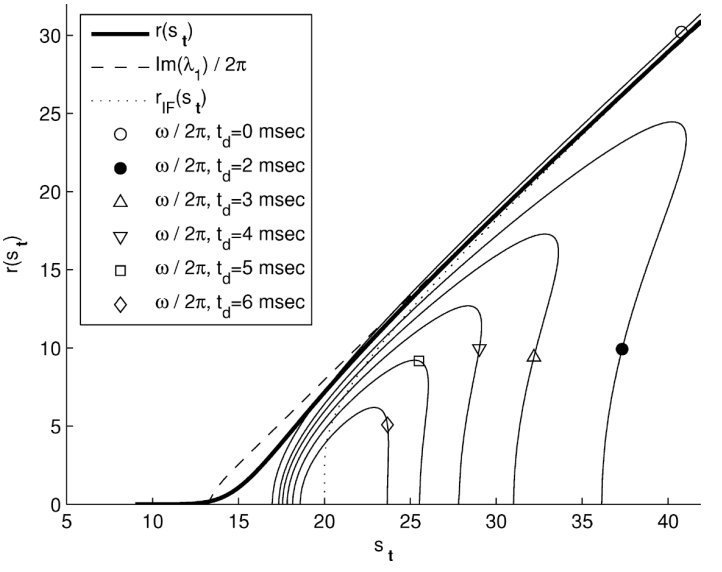

Figure 4. Firing rate, r, versus current, s, the heavy continuous line, calculated numerically. Dotted curve is firing rate of Equation 1 for non-stochastic and constant s, $r_{if}(s_t)$, for which there is no firing for $s < \gamma$, $\gamma = 20$ is the nominal value in all plots. Both curves asymptote to $r = s - \gamma/2$, not shown. Remaining plots, described in the text, are *frequencies*, and have the same dimensions as $r(s_t)$.

in the (s_t, G)-plane an infinitesimal increment in input s^e produces an unbounded increment in output s_t, thus implying instability, a fact which will be demonstrated more formally later. This behavior is also clear from the plots in Figure 6. The plot of Equation 25, in the (s_t, G)-plane, is shown as the heavy solid line in Figure 6A, from which it is clear that there is a minimum value of G, below which this instability disappears.

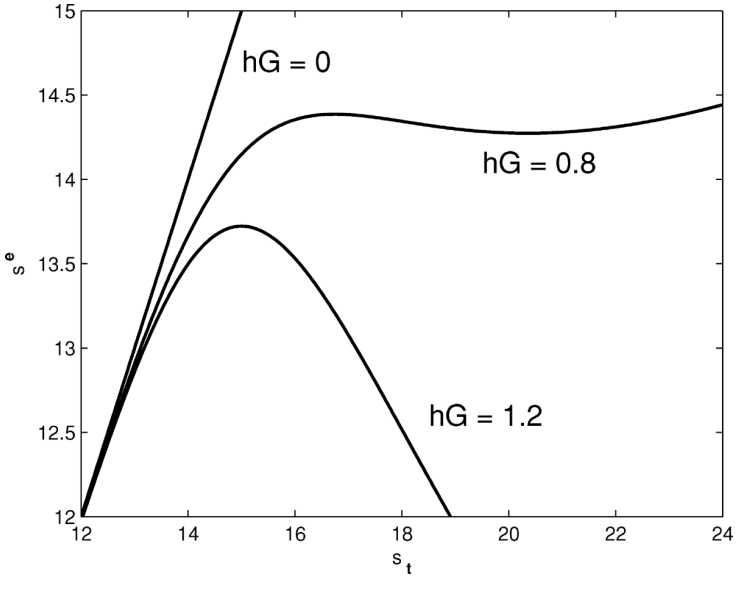

Figure 5. s^e versus s_t, (23), for $g = hG = 0$, 0.8 and 1.2. As explained in the text instability occurs at the stationary points.

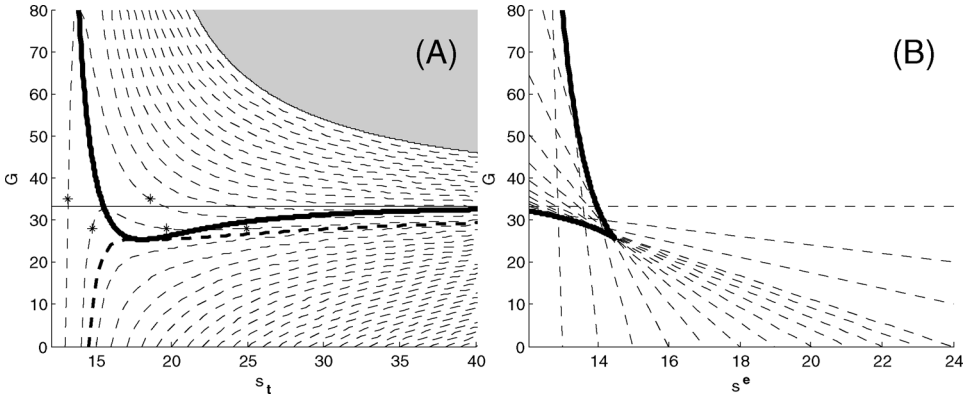

Figure 6. (A) Equation 25, is plotted as a heavy continuous line, with minimum at s_t^*, the inflexion-point value of $r(s_t)$, (28). s^e = constant in (26), are shown as thin dashed lines, with the value of s^e given by the intersection at $G = 0$. $hG = 1$, plotted as a horizontal thin line, is the asymptote of all dashed lines, as well as Equation 25. The heavy line meets each dashed curve in an extremum, as required by Equation 24, and heavy dashed curve in a second order contact, see text. For $G = 35$ and $s^e = 13$ there are two equilibria indicated by asterisks; and for $G = 28$ and $s^e = 14$, there are three equilibria indicted by asterisks. (B) The corresponding (s^e, G)-plane. The thin straight lines represent s_t = constant in Equation 26 where the constant is given by the intersection at $G = 0$. The envelope of these is the cusp, which is analytically determined by Equation 30. As shown later no equilibria exist for $G > 1/h$, to the right of the cusp of (B).

We can rewrite Equation 23 as

$$G = \frac{s_t - s^e}{hr(s_t)}, \tag{26}$$

and Figure 6A contains plots of (26) for constant s^e, as dashed lines. Note that for a given value s^e, each curve originates at $s^e = s_t$, where $G = 0$. Since $r(s_t) \sim s_t$ for s_t large, (see Figure 4), it follows from Equation 26 that in Figure 6 all s^e = constant curves asymptote to $1/h$. Differentiating Equation 26, for s^e constant yields

$$\left(\frac{\partial G}{\partial s_t}\right)_{s^e} = \frac{1}{hr}\left\{1 - (s_t - s^e)\frac{r'}{r}\right\}. \tag{27}$$

On equating the values of G in Equation 25 and 26, we see that 27 vanishes at points of intersection of 26 with 25.

Also indicated in Figure 6A is the gray region above $G = s_t/(hr(s_t))$ which marks the boundary of admissability in the plane, since $s^e \geq 0$ is a precondition of the problem.

Geometrical considerations

As mentioned, an equilibrium solution, for a fixed total current, s_t, represents the family of solutions given by Equation 19. On the other hand, the dynamical solution of equation, requires specification of external current s^e and gain G, so that s_t is not known before solution. We therefore also consider the (s^e, G)-plane. In this regard, we note that equation, takes on a minimum value at the inflection point of $r(s_t)$, denoted by s_t^*,

$$r''(s_t^*) = r''_* = 0$$
$$g_* = hG_* = 1/r'_*, \tag{28}$$

which will play an important role in the following. If we define

$$s_*^{\mathbf{e}} = s_{\mathbf{t}}^* - G_* r(s_{\mathbf{t}}^*) \tag{29}$$

then the curve of $s^{\mathbf{e}} = s_*^{\mathbf{e}}$ in the $(s_{\mathbf{t}}, G)$-plane, indicated in Figure 6A by heavy dashes, passes through $(s_{\mathbf{t}}^*, G_*)$ with zero first and second derivatives. Also clear from this figure is the observation that for $1/r'_* < hG$, the curves of constant $s^{\mathbf{e}}$, take on extrema at their intersection with Equation 25.

Figure 6A clearly indicates that for a fixed value of G, a horizontal line, there can be one, two or three intersections with curves of constant $s^{\mathbf{e}}$. Thus, a point $(s^{\mathbf{e}}, G)$ in the $(s^{\mathbf{e}}, G) \geq 0$ quadrant of possible initial *states* can be associated with one, two or three different equilibria, with G_*, the minimal gain for which there exists more than one equilibrium. Figure 6B, which depicts the $(s^{\mathbf{e}}, G)$-plane illustrates this non-uniqueness . Equation 23 states that loci of constant $s_{\mathbf{t}}$ are straight lines of negative slope. The multi-valuedness, which is intimately related to stability, manifests itself in the cusp that is evident in Figure 6B.

Analytically, the cusp locus is obtained as the envelope of the straight lines of (23, $s_{\mathbf{t}}$ constant). In parametric form, this (Courant 1936) is given by

$$\left.\begin{aligned} g = hG &= 1/r'(s_{\mathbf{t}}) \\ s^{\mathbf{e}} &= s_{\mathbf{t}} - r(s_{\mathbf{t}})/r'(s_{\mathbf{t}}) \end{aligned}\right\}, \tag{30}$$

this first of which is just (25). It follows from Equation 28 that $dg/ds_{\mathbf{t}} = 0 = ds^{\mathbf{e}}/ds_{\mathbf{t}}$ at $s_{\mathbf{t}} = s_{\mathbf{t}}^*$, which locates the cusp at $(s_*^{\mathbf{e}}, G_*)$. The cusp locus, Equation 30, is indicated in the $(s^{\mathbf{e}}, G)$ plane of Figure 6B. Some insight into the cusp geometry results from the local approximation to $s_{\mathbf{t}} = s_{\mathbf{t}}(s^{\mathbf{e}}, g)$ near $(s_*^{\mathbf{e}}, g_*)$, given by

$$s^{\mathbf{e}} - s_*^{\mathbf{e}} = \frac{|r'''_*|}{6r'_*}(s - s_{\mathbf{t}}^*)^3 - (g - g_*)\{r_* + r'_*(s - s_{\mathbf{t}}^*)\}, \tag{31}$$

from which the cusp is locally determined by,

$$s^{\mathbf{e}} - s_*^{\mathbf{e}} = (g - g_*) \pm \frac{2}{3}(r'_*)^2 \sqrt{\frac{2}{|r'''_*|}}(g - g_*)^{3/2}. \tag{32}$$

For future reference we observe that the upper equation of 30 is just 25, and therefore this curve maps to the cusp of Figure 6B; $s_{\mathbf{t}} > s_0^*$ maps to the lower branch, and $s_{\mathbf{t}} < s_0^*$ to the upper branch of the cusp.

In Figure 7, we present the combined features of Figures 6A and 6B as the surface $s_{\mathbf{t}} = s_{\mathbf{t}}(s^{\mathbf{e}}, G)$. From Equation 23, for $0 \leq s_{\mathbf{t}} \leq \infty$, $s_{\mathbf{t}}$ is constant on straight lines of negative slope, $-1/(hr(s_{\mathbf{t}}))$, originating at $s^{\mathbf{e}} = s_{\mathbf{t}}$, where $G = 0$. $s_{\mathbf{t}}(s^{\mathbf{e}}, G)$ is thus a ruled surface. The dashed curves of Figure 6(A) imply that vertical lines of Figure 6(B) for $s^{\mathbf{e}} > s_*^{\mathbf{e}}$ terminate at $G = 1/h$; and for $s^{\mathbf{e}} < s_*^{\mathbf{e}}$ they turn through 180° at the upper limb of the cusp, then turn again by 180° at the lower limb before terminating at $G = 1/h$. Hence, Figure 6B may be regarded as the *collapse* of all horizontal slices of the surface onto a horizontal plane. Similarly Figure 6A, can be regarded as the collapse of vertical slices, $s^{\mathbf{e}} =$ constant, onto a vertical plane. This multi-valuedness of the surface is sometimes referred to as a *cusp catastrophe* (Arnold 1986).

It is worth pausing to point out that discussion of this and the last section has general application. Although the figures drawn, Figures 6 and 7, depend on the particular form of $r(s_{\mathbf{t}})$ obtained from solving our population equation, the general structural features appear for any realistic $r(s_{\mathbf{t}})$ as in Figure 1, which has an inflection point.

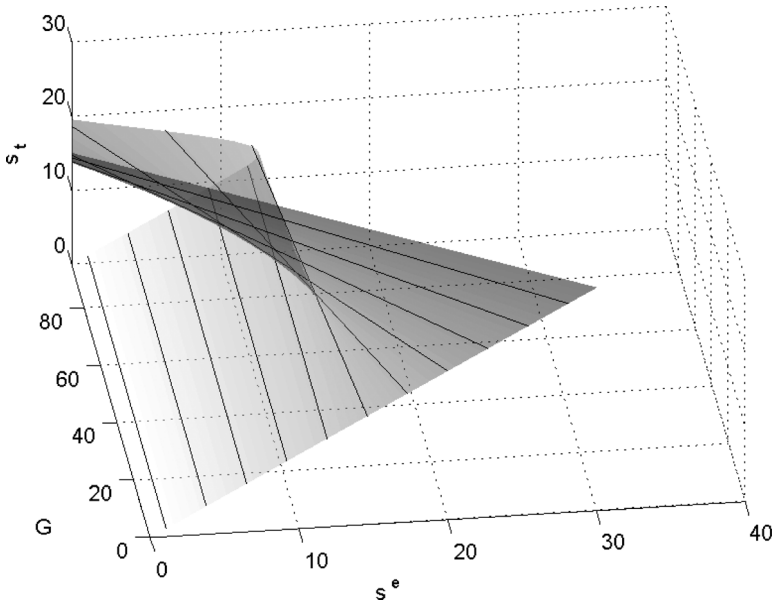

Figure 7. The surface $s_{\mathbf{t}} = s_{\mathbf{t}}(s^{\mathbf{e}}, G)$, as generated by Equation 19. The surface can have as many as three sheets above points of the $(s^{\mathbf{e}}G)$-plane.

Eigenfunction analysis

As preparation for the formal stability analysis, we consider the eigentheory of L, (7), as characterized by

$$\left.\begin{array}{c} L\phi_n = \lambda_n \phi_n \\ \mathcal{J}[\phi_n] \mid_{v=0} = \mathcal{J}[\phi_n]|_{v=1} \\ \phi_n(1) = 0. \end{array}\right\} \tag{33}$$

in which s is a constant. Since L is a real operator, complex eigenvalues occur in pairs, i.e., $[\lambda_n, \phi_n]$ and $[\lambda_n^*, \phi_n^*]$. The eigenfunction ϕ_0 corresponding to

$$\lambda_0 = 0 \tag{34}$$

is the equilibrium solution, U, examples of which are shown in Figures 2 and 3.

In order to investigate the stability of equilibrium it is useful to also consider the related adjoint problem

$$L^\dagger \widehat{\phi}_n = \lambda_n^* \widehat{\phi}_n, \tag{35}$$

(see Sirovich (2003)). $L^\dagger$ is defined so that under appropriate boundary conditions

$$(L^\dagger \widehat{\phi}, \phi)_v = (\widehat{\phi}, L\phi)_v. \tag{36}$$

As shown in the cited reference

$$L^\dagger \widehat{\phi} = \begin{cases} -\gamma v \frac{\partial}{\partial v}\widehat{\phi} - s[\widehat{\phi}_n(v) - \widehat{\phi}_n(v-h)]/h; \ 0 \le v < 1-h \\ -\gamma v \frac{\partial}{\partial v}\widehat{\phi} - s[\widehat{\phi}_n(v) - \widehat{\phi}(0)]/h; \ 1-h \le v \le 1 \end{cases} \tag{37}$$

and the adjoint boundary condition is given by

$$\widehat{\phi}_n(0) = \widehat{\phi}_n(1). \tag{38}$$

The sets $\{\phi_n\}$ and $\{\widehat{\phi}_n\}$ are bi-orthogonal and we take them to be normalized so that

$$(\widehat{\phi}_n, \phi_m) = \delta_{nm}. \tag{39}$$

Details of the derivations and illustrations of $\{\lambda_n\}$, $\{\phi_n\}$ and $\{\widehat{\phi}_n\}$ can be found in the cited reference.

The spectrum, $\{\lambda_n\}$, of L, which is interesting its own right, also figures in the subsequent deliberations, and is now informally discussed for a variety of input currents.

To start, we observe that for $s \approx 0$, we have

$$L(\phi) \approx \gamma \frac{\partial}{\partial v}(v\phi), \tag{40}$$

and from this

$$L(v\phi) \approx \gamma v \frac{\partial}{\partial v}(v\phi) = \gamma \frac{\partial}{\partial (lnv)}(v\phi). \tag{41}$$

In this limit the operator is purely translational, from which it follows that the spectrum is continuous and lies on the (vertical) imaginary axis (Friedman 1990) but with boundary conditions becomes discrete. In Figure 8, we show a series of spectra for $s > 0$. All of these correspond to an equilibrium shown in Figure 3. The near vertical locus in Figure 8A, $s/\gamma = .5$ evolves from the continuous spectrum that lies on the imaginary axis when $s = 0$. To understand why the real spectrum is uniformly distributed, we note that from Figure 3 the equilibrium solution at $s/\gamma = .5$, the solution falls to zero (exponentially) as the boundaries are approached. In view of this, for s small; if we expand in small h ($h = 0.03$

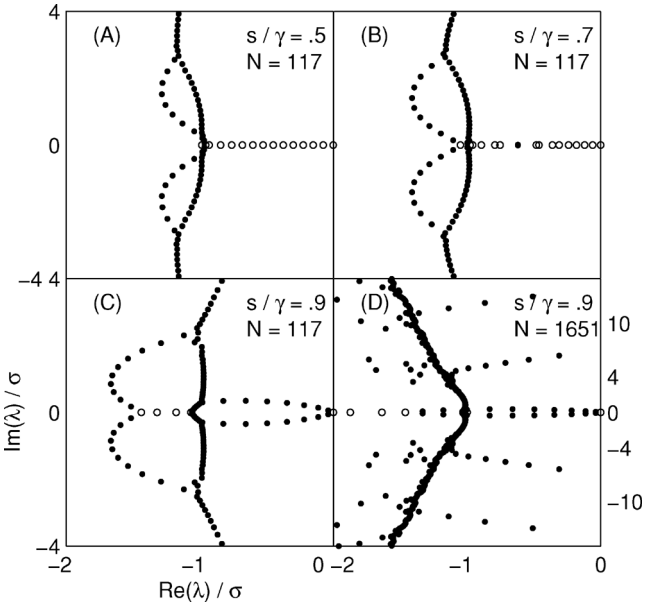

Figure 8. Spectra of L normalized by the synaptic arrival rate, σ, see Equation 42, with abscissa and ordinate shown in lower left. (A) $s/\gamma = .5$, note that the real eigenvalues (unfilled circles) are uniformly distributed. Complex eigenvalues (filled circles) occur as conjugate pairs; (B) $s/\gamma = .7$, real eigenvalues show pairwise coalescence, note one pair has become a complex pair; (C) $s/\gamma = .9$, note full coalescence into conjugate pairs and the reverse occuring at the left; (D) higher resolution display for $s/\gamma = .9$, observe change in vertical scale. Note each panel displays only a partial collection of eigenvalues.

in our computations)

$$\mathcal{L}\phi = \frac{1}{\sigma} L\phi \approx \frac{\gamma}{\sigma}\frac{\partial}{\partial v}\{(\gamma v - s)\phi\} + \frac{h^2}{2}\frac{\partial^2}{\partial v^2}\phi, \tag{42}$$

since division by σ proves to be a suitable normalization. The operator on the right of Equation 42 is the Ornstein-Uhlenbeck operator, and its adjoint is the Hermite operator (Gardiner 1983), which is known to have equally spaced eigenvalues. As mentioned for s small the solution does not *feel* the boundaries, which applies to $s/\gamma = .5$, and offers an explanation for the uniformity of the real eigenvalues. In Figure 8B, $s/\gamma = .7$, the real eigenvalues have begun migrating to one another and in fact one pair has coalesced and bifurcated into a conjugate pair. In Figure 8C $s/\gamma = .9$, and all eigenvalues to the right of the continuous spectrum have become conjugate pairs, except for the zero eigenvalue, the eigenfunction of which is shown in Figure 3. These three figures have been determined on the basis of a relatively coarse grid of 117 intervals in membrane potential. In Figure 8D we show a portion of the spectrum when $s/\gamma = .9$, derived from the indicated fine grid. As can be seen the spectrum is greatly enriched. Note that the ordinate of Figure 8D, unlike the other plots, has the range $(-15, 15)$.

Within the framework of the diffusion model, Knight (2000), draws an interesting analogy with limulus results (Knight 1972), for which $\lambda_n = in\omega(s) - n^2\gamma(s)$ (see Knight (2000) for details), a form also suggested by Abbott and van Vreeswijk (1993), see also Treves (1993). At sufficiently large s, this *parabolic* spectral distribution, approximates the principal eigenvalues, i.e., those in the neighborhood of the origin of Figure 8. However, as is clear from Figure 8D, the operator L, Equation 7 has a far richer spectrum. Other shortcomings of the diffusion approximation have been mentioned in Tuckwell and Cope (1980), Wilbur and Rinzel (1982) and Sirovich (2003).

Knight (2000) presents a general stability analysis, and in the following section we are able to present a more refined stability analysis which follows from the specific operator, Equator 7, and in particular from the appearance of the total input current $s_{\mathbf{t}}$ as a linear coefficient in that operator.

Stability problem

To investigate the stability of the equilibrium solution, Equation 18, we consider the perturbed solution

$$\rho = U + \epsilon u(v, t), \tag{43}$$

under the constraint that $s_{\mathbf{t}}$ is fixed. Here ϵ represents the usual formal small parameter. If Equation 43 is substituted into 15 then to order ϵ

$$\frac{\partial u}{\partial t} = \gamma\frac{\partial}{\partial v}vu - \frac{s_{\mathbf{t}}}{h}\{u(v) - u(v-h)\} + g\frac{1}{h}\{U(v-h : s_{\mathbf{t}}) - U(v : s_{\mathbf{t}})\}r_1 \tag{44}$$

with perturbed firing rate

$$r_1 = \frac{s_{\mathbf{t}}\int_{1-h}^{1} u(v)dv/h}{1 - kG}. \tag{45}$$

with k given by Equation 14. If we define

$$H = \begin{cases} 0;\ 0 \le v \le 1-h \\ 1;\ 1-h < v \le 1 \end{cases} \tag{46}$$

then $k = (H, U)$, and inner product, is seen to be a one dimensional projection. In these terms, Equation 44 can be written as

$$\frac{\partial u}{\partial t} = Lu + \frac{Gs_{\mathbf{t}}(H, u)}{h(1 - kG)}\{U(v - h : s_{\mathbf{t}}) - U(v : s_{\mathbf{t}})\}. \tag{47}$$

For exponential solutions in the time domain

$$u \propto e^{\mu t}, \tag{48}$$

it follows that

$$\mu u = Lu + \Phi(v)\frac{G}{1 - kG}(H, u) \tag{49}$$

with

$$\Phi(v) = \frac{s_{\mathbf{t}}}{h}\left\{U(v - h : s_{\mathbf{t}}) - U(v : s_{\mathbf{t}})\right\}, \tag{50}$$

and L given by Equation 7. Clearly u must satisfy the same boundary conditions as ρ, viz., Equations 9 and 10, which with 49 and 50 specifies the *stability problem*. A key feature of Equation 49 is that the perturbation to L, is just a one-dimensional projection, namely the last term on the right hand side of Equation 49, proportional to (H, u).

Solution

To solve Equation 49 we employ the eigenfunctions $\{\phi_n\}$, Equation 33, and adjoint eigenfunctions $\{\widehat{\phi}_n\}$, Equation 35, which form bi-orthonormal sets, Equation 39. The inner product of Equation 49 with $\widehat{\phi}_l$ yields,

$$\mu(\widehat{\phi}_l, u) = \lambda_l(\widehat{\phi}_l, u) + \frac{G(H, u)}{1 - kG}(\widehat{\phi}_l, \Phi), \tag{51}$$

which in turn gives

$$(\widehat{\phi}_l, u) = \frac{1}{\mu - \lambda_l}\frac{G(H, u)}{1 - kG}(\widehat{\phi}_l, \Phi). \tag{52}$$

Since

$$u = \sum_l (\widehat{\phi}_l, u)\phi_l(v), \tag{53}$$

it follows that the projection operator applied to any element u in the space, is given by $(H, u) = \sum_l (\phi_l, u)(H, \phi_l)$, and therefore if we multiply Equation 52 by (H, ϕ_l) and sum on the index l we obtain

$$\sum_l (H, \phi_l)(\widehat{\phi}_l, u) = (H, u) = \frac{G}{1 - kG}(H, u)\sum_l \frac{(H, \phi_l)(\widehat{\phi}_l, \Phi)}{\mu - \lambda_l}. \tag{54}$$

From this, the *dispersion relation* for the stability exponent μ follows,

$$1 = \frac{G}{1 - kG}\sum_l \frac{(H, \phi_l)(\widehat{\phi}_l, \Phi)}{\mu - \lambda_l}. \tag{55}$$

Once this is solved for μ, the calculation is finished by determining the corresponding u. Thus, we substitute Equation 52 into 53 to obtain

$$u = \frac{G}{1 - kG}(H, u)\sum_l \frac{(\widehat{\phi}_l, \Phi)}{\mu - \lambda_l}\phi_l(v). \tag{56}$$

Since u is indeterminate up to a multiplicative constant, and it proves formally convenient to take $(H, u) = 1$,
so that

$$u(v) = \frac{G}{1 - kG} \sum_l \frac{(\widehat{\phi}_l, \Phi)}{\mu - \lambda_l} \phi_l(v), \tag{57}$$

which completes the formal solution.

Criterion for instability

We recall that $U = \phi_0$ is the eigenfunction associated with $\lambda_0 = 0$ for a particular net current $s_{\mathbf{t}}$. As easily verified the corresponding adjoint eigenfunction is a constant which we can take to be $\widehat{\phi}_0 = 1$. It then follows from integrating Equation 17 across the interval $v = (0, 1)$ that

$$(\widehat{\phi}_0, \Phi) = \int_0^1 \Phi(v) dv = 0. \tag{58}$$

Next, we observe that the quantities which appear in Equation 55,

$$C_l = (H, \phi_l)(\widehat{\phi}_l, \Phi), \tag{59}$$

are, for all l, known once $s_{\mathbf{t}}$ is specified, since $s_{\mathbf{t}}$ fully specifies the equilibrium, Equation 17, as well as the eigentheory 33 and 37. In these terms Equation 55 is given by

$$1 = \frac{G}{1 - kG} \sum_{l \neq 0} \frac{C_l}{\mu - \lambda_l}. \tag{60}$$

The term $l = 0$ is omitted from the summation since $C_0 = 0$ from Equation 58. It is convenient to rearrange the dispersion relation, Equation 60, in the form

$$G = \left(k + \sum_{l \neq 0} \frac{C_l}{\mu - \lambda_l} \right)^{-1}. \tag{61}$$

The case of time delay

A real neuron experiences a variety of signaling delays due to synaptic events, transmission times, refractoriness and related factors. To explore this we can lump the various causes of lag into a single delay time, t_d, so that the incoming response felt by a neuron is delayed, $r = r(t - t_d)$. The analysis which is almost immediate, is briefly outlined in Appendix 2. The dispersion relation then becomes

$$G = e^{\mu t_d} \left(k + \sum_{l \neq 0} \frac{C_l}{\mu - \lambda_l} \right)^{-1}, \tag{62}$$

a form which subsumes Equation 61.

Critical locus

Instability of the equilibrium solution, $U(v : s_{\mathbf{t}})$ takes place when μ passes from the negative, $Re\mu < 0$, to the positive, $Re\mu > 0$, complex half plane. Thus, the critical stability boundary is obtained when μ is pure imaginary, $\mu = i\omega$. If this is substituted into Equation 62, the

critical locus is determined by

$$G = e^{i\omega t_d}\left(k + \sum_{l\neq 0} \frac{C_l}{i\omega - \lambda_l}\right)^{-1}. \tag{63}$$

The roots of the imaginary part of Equation 63,

$$0 = Im\left[e^{i\omega t_d}\left(k + \sum_{l\neq 0} \frac{C_l}{i\omega - \lambda_l}\right)^{-1}\right], \tag{64}$$

determine the critical frequencies. Since the values of k, C_l and λ_l are determined by the net current, $s_{\mathbf{t}}$, and since Equation 64 is an even function of ω, the roots of 64, ω, can be expressed as

$$\omega(s_{\mathbf{t}}) = \pm\Omega(s_{\mathbf{t}}). \tag{65}$$

The critical gain is then determined by substitution of Equation 65 into the real part of 63.

$$G = Re\left[e^{i\Omega(s_{\mathbf{t}})t_d}\left(k + \sum_{l\neq 0} \frac{C_l}{i\Omega(s_{\mathbf{t}}) - \lambda_l}\right)^{-1}\right] = \Gamma(s_{\mathbf{t}}). \tag{66}$$

Other applications of Equation 62 will be given below.

Results and discussion

We start discussion with the case of zero delay. For $\omega = 0$, Equation 64 is identically satisfied since the terms of the summation occur in conjugate pairs. Thus, for each value of $s_{\mathbf{t}}$, Equation 62 with $\mu = 0$ determines a value of G at which instability occurs. But, as a little thought reveals, and calculation verifies, this must be the same as equation. Hence, this implies

$$-\sum_{l\neq 0} C_l/\lambda_l = hr'(s_{\mathbf{t}}) - h\frac{r(s_{\mathbf{t}})}{s_{\mathbf{t}}} = hs_{\mathbf{t}}\frac{d}{ds_{\mathbf{t}}}\left(\frac{r(s_{\mathbf{t}})}{s_{\mathbf{t}}}\right), \tag{67}$$

a non-obvious identity, in which we have used $k = hr(s_{\mathbf{t}})/s_{\mathbf{t}}$, Equation 14. For future reference, it should be noted that the root $\omega = 0$ also satisfies Equation 63 independently of time delay.

Recall that the stability boundary, Equation 25, maps into the cusp shown in Figure 6B: $s_{\mathbf{t}} > s_{\mathbf{t}}^*$ is the lower branch; and $s_{\mathbf{t}} < s_{\mathbf{t}}^*$ the upper branch, and hence the region lying between $hG = s_{\mathbf{t}}/r(s_{\mathbf{t}})$, Equation 25 and $hG = 1/r'(s_{\mathbf{t}})$, the gray boundary of Figure 6A, maps into the cusp region of Figure 6B. Inspection of this figure or Figure 7 indicates there are either two or three equilibria at locations $(s^{\mathbf{e}}, G)$ in the cusp region. In crossing the $\omega = 0$ locus, the stability exponent, μ, passes across the imaginary axis as a real number, and this, loosely speaking, implies a saddle-node bifurcation (Guckenheimer & Holmes 1983). Therefore, an equilibrium solution can be expected to lose stability. In fact, calculation shows that only the lowest possible value of $s_{\mathbf{t}}$ corresponds to a stable equilibrium, which appears to be a global attractor. For example, in Figure 6A at $G = 35$, two possible equilibria exist for $s^{\mathbf{e}} = 13$, shown as asterisks. Numerical solution of Equation 15 (or calculations based on 62) shows that the left most equilibrium solution is stable, and any perturbation of the right most equilibrium leads to an exponential relaxation to the left equilibrium. For $G = 28$ and $s^{\mathbf{e}} = 14$, there are three possible equilibria, shown as asterisks in Figure 6A, and the two right most equilibria both relax to the left most equilibrium. Thus, if several states are possible, the lowest firing rate state is the global attractor. This appears to be the general rule, even

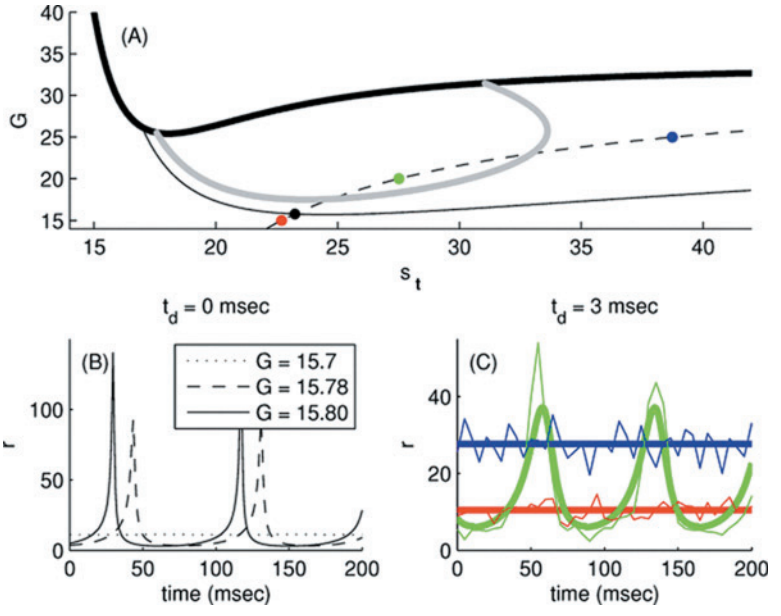

Figure 9. (A) The critical gain when $\omega = 0$, Equation 25, is plotted as a heavy black line; the critical gain, Equation 66, for $t_d = 0$, $\omega \neq 0$, is plotted as a thin black line; the critical gain for $t_d = 3$ msec, is plotted as a gray line; the dashed line is the locus, (26), for $s^e = 18$; (B) Firing rate behavior in the neighborhood of the black dot in Figure 9(A), for $t_d = 0$. Values of G are given in the inset. Note the firing rate for $G = 15.78$ has been offset for illustration; (C) Calculation of firing rate behavior, for lag time $t_d = 3$ msec, at the three color coded points in (A). Irregular traces come from direct simulation of 1000 neurons at the same parameter values.

for synchrony, discussed next. In the case of *large* time delays, discussed later, there can be multiple stable asynchronous states.

Oscillations

In addition to the root $\omega = 0$, solution of Equation 64 yields a pair of conjugate roots $\pm\,\Omega(s_t)$ Equation 66. The corresponding critical value for the gain G, 66, is shown in Figure 9A. The critical frequency of oscillations, $\omega(s_t)/2\pi = \Omega(s_t)/2\pi$, is plotted in Figure 4, as the curve distinguished by an open circle. Figure 4 also compares $r(s_t)$ and the imaginary part of the first complex eigenvalue, $Im(\lambda_1)/2\pi$. On dimensional grounds, the three loci might be expected to lie in close proximity, and this is seen to be the case in Figure 4. The relevant time scale of the problem is set by the reciprocal of the interspike interval $r(s_t)$, and the oscillation frequency, $\Omega(s_t)/2\pi$, Equation 65, can reasonably be assumed to be of the same order. Since resonance furnishes the mechanism for instability, this should occur when the frequency $Im(\lambda_1)/2\pi$, of the pole closest to the imaginary axis, lies within reach of $r(s_t)$. Equivalently, the eigenfunction with eigenvalue closest to the imaginary axis can be reasonably supposed to be the most unstable.

Knight (2000) arrives at forms similar to Equation 61 and 62, and offers an interesting qualitative analysis, based on a one term approximation of the summation in Equation 63 which retains the term containing the eigenvalue closest to the imaginary axis, λ_1. As foreshadowed by Figure 4, since ω, given by Equation 65, and $Im\ \lambda_1$ lie close to one another, thus the critical frequency is well approximated, while the critical gain is inaccurate unless stochastic influences are small, as when the net current s_t is large.

The passage across the stability boundary is a supercritical Hopf bifurcation (Kuramoto 2003), as has been noted in related prior studies (Kuramoto 1991; Brunel & Hakim 1999). Perturbation beyond the infinitesimal leads to a Landau equation for the amplitude of the oscillation (Kuramoto 2003). We forgo the usual lengthly derivation of the amplitude equation, especially in view of the near singular behavior we next describe. In Figure 9A we indicate by a black dot a neighborhood of the $t_d = 0$ stability boundary, where we inspect the behavior of the three close values of G indicated in the inset of Figure 9B. For $G = 15.7$, the firing rate, $r(t)$, settles down to equilibrium with a decrementing oscillation at a frequency $\Omega(s_t)/2\pi \approx r(s_t)$. At the two higher values of G, steady state oscillations set in at virtually the same frequency. Note that the peak amplitude, $A(s)$ undergoes extreme growth for slightly increased gain G. Since simple scaling arguments suggest that $\triangle A \propto (\triangle G)^{1/2}$, our discussion implies that the proportionality constant is large. Calculation shows that the integrated number of nerve impulses over, say, one period of each of the three time histories is roughly the same, which is reasonable since (s_t, G) is virtually identical for the three cases. The rapid growth of amplitude with G strongly suggests that the neurons become clocklike, and near phase-locked, as the stability boundary is passed.

Non-zero time delay

In discussing the effects of time delay, we recall that time drops out of the problem at equilibrium, and so the deliberations based on Figure 6 still apply. Figure 9 also displays the stability boundary calculated for a time delay of 3 msec, based on Equation 66, and in Figure 10 we plot a range of these critical boundaries based on 66. As seen, in Figure 10, the domain of synchronous activity diminishes as t_d increases. Another consequence of a

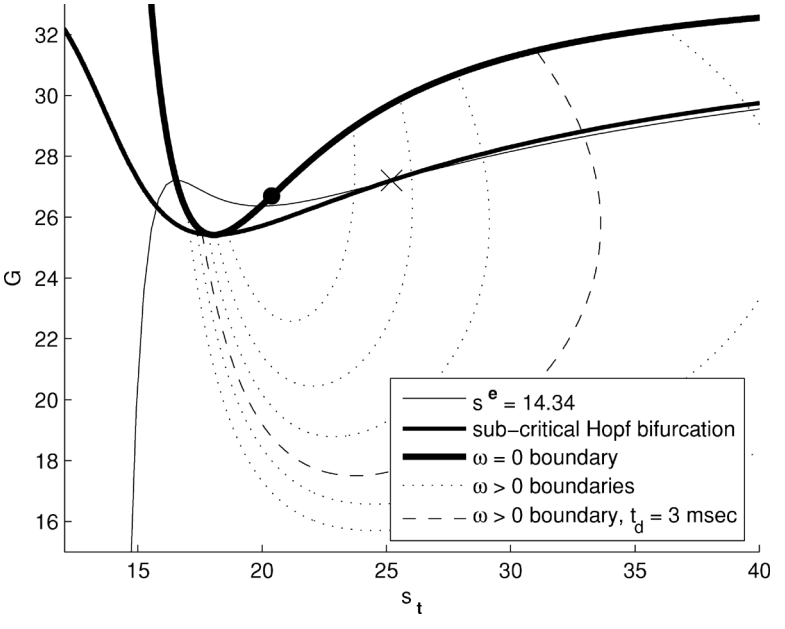

Figure 10. Stability boundaries for $t_d = 2, 3, 4, 5, 6$ msec are shown as dotted (or dashed) curves which enclose decreasing areas. The corresponding oscillation frequencies are shown on Figure 4. As explained in the text, the heavy continuous curve is the boundary across which synchronous activity is lost. The "sub-critical Hopf bi-furcation curve" maps to the cusp of Figure 6(B), but arises from single valued sheets of Figure 7.

non-zero time lag, t_d, is that for fixed $s_{\mathbf{t}}$, the stability boundary, Equation 66, can become double valued. Thus, in Figure 10 there are values of $s_{\mathbf{t}}$, and stability boundaries, such that for increasing G, we can move through an asynchronous region until the stability boundary is encountered, after which synchronous activity appears, and on further increasing G we again encounter the stability boundary, after which synchrony disappears. If we further increase G, we encounter the $\omega = 0$ critical locus. Figure 9C indicates the transition from asynchrony to synchrony to asynchrony as we proceed on Equation 26, $s^{\mathbf{e}} = 18$, for $t_d = 3$ msec. The three calculations at $G = 15, 20, 25$ were confirmed by direct simulation, Equation 15, which we discuss later. The rapid amplitude growth across the stability boundary, seen for $t_d = 0$, is now gone. Thus, the tendency toward phase locked, clocklike neurons, is removed by the introduction of time delay.

The loci of critical frequencies $\Omega(s_{\mathbf{t}})$, Equation 65, for the various time delays, t_d, are plotted in Figure 4. For fixed net current $s_{\mathbf{t}}$, multivaluedness in $\Omega(s_{\mathbf{t}})$ is seen in these plots. Perhaps a more striking feature is that $\Omega(s_{\mathbf{t}})/2\pi$, unlike when $t_d = 0$, can depart very significantly from $r(s_{\mathbf{t}})$. Thus, the period of oscillation that is set up in passing the critical boundary is no longer simply related to the interspike interval, as is the case when $t_d = 0$.

To illustrate the range over which time delay affects synchronous behavior, we plot in Figure 10 the stability boundaries for various time delays. For the nominal values at which we perform our calculations, $h = .03$ and $\gamma = 20$, there is a critical time delay at which synchrony is lost, $t_d = 7.38$ msec, indicated by the *dot* on the thick curve at $s_{\mathbf{t}} = 20.387$, $G = 26.693$.

A striking feature of $t_d \neq 0$ is the mismatch of typical oscillation periods, $2\pi/\Omega(s_{\mathbf{t}})$ with the delay time, t_d, as seen in Figure 4. Typically, t_d is at least an order of magnitude smaller than $2\pi/\Omega(s_{\mathbf{t}})$. This is consistent with the earlier observation that a relatively slight delay, t_d, interferes with phase locking. This is underlined by the amplitude changes exhibited in Figure 9B and C in going from $t_d = 0$ to $t_d = 3$ msec. The above mentioned narrow range of possible time delays at which synchrony can occur may be of significance in a larger context if, as had been suggested in the literature, synchrony is a desirable state for certain neural activities.

Another aspect which bears mention (and which also carries over to the case of zero time delay) concerns the difference in the way features appear in the two planes of Figure 6. The locus of the cusp shown in Figure 6B maps to the loci of points in the ($s_{\mathbf{t}}$, G)-plane where equilibria first become two valued. One of these loci must be the $\omega = 0$ curve, Equation 25, in the ($s_{\mathbf{t}}$, G)-plane, since this maps to the cusp itself. The inverse map of the second locus, parametric in the net current $s_{\mathbf{t}}$, is shown as an intermediate weight curve in Figure 10. For reasons given below, this is referred to as the subcritical Hopf bifurcation boundary. This locus is interesting since it lies in a zone where limit cycle behavior is indicated. In a very general sense, a limit cycle may be regarded as *orbiting* motion around the equilibrium solution about which perturbation takes place. But at the *subcritical Hopf bifurcation line* in Figure 10, this unperturbed equilibrium would lose stability to the equilibrium at the lower firing rate. And indeed it is found that beyond this line, the limit cycle disappears and a solution started near this equilibrium goes to the other equilibrium. This behavior follows what is termed a sub-critical Hopf bifurcation (Strogatz 2000).

To illustrate this behavior, we follow the passage of a population of neurons for which $s^{\mathbf{e}} = 14.34$, and $t_d = 3$ msec. In effect, we consider the intersection of the surface in Figure 7 with $s^{\mathbf{e}} = 14.34$. This curve is shown in Figure 11. Starting at the upper right of the figure we have a continuous line, indicating stable equilibria (asynchronous), until ($s_{\mathbf{t}}$, G) $\approx$ (32.8, 28.65), the point at which the thin line of Figure 10 crosses the $t_d = 3$ msec, stability boundary. The loss of stability is indicated by the dashed line in Figure 11. This transition, a supercritical

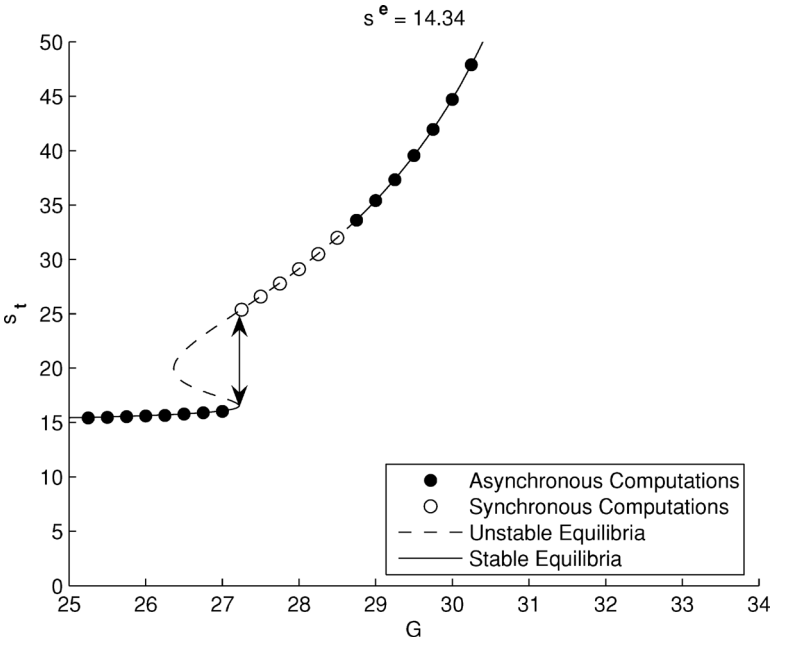

Figure 11. Section of Figure 7 taken at $s^{\mathbf{e}} = 14.34$. Continuous lines locate stable equilibria. Dashes signify unstable equilibria. Filled circles indicate calculation confirming stable equilibria, and open circles, calculations confirming limit cycle behavior. Time delay, $t_d = 3$ msec.

Hopf bifurcation, marks the start of limit cycle (synchronous) behavior. The open circles indicate confirmation of this by integration of Equation 15 at the indicated values. (Filled circles indicate stable equilibria confirmed by integrating Equation 15.) Limit cycle behavior continues until the thin line of Figure 10 crosses the medium line, indicated by $\times$, when $(s_{\mathbf{t}}, G) \approx (25.26, 27.22)$. This is also the location at which the surface in Figure 7 becomes double valued, i.e., it has a vertical tangent. As already mentioned, equilibria on the lower surface become global attractors. Thus, limit cycle behavior becomes unstable, and the solution *jumps* to equilibrium at $(s_{\mathbf{t}}, G) \approx (16.56, 27.22)$, indicated by a double arrow in Figure 11 since this subcritical Hopf bifurcation goes in both directions. Following this curve to lower values of G occurs only through equilibria. Note that the other vertical tangent in Figure 11 plays no role.

Large time delay

Unlike what has been described above, Fusi and Mattia (1999), using a much simplified population model, found two stable asynchronous solutions. With thanks to the referee who pointed this out, we explored this possibility when the delay, t_d, exceeded the above mentioned critical value of $t_d = 7.38$, at which point oscillations disappear. In this case, we can solve equation under the hypothesis that oscillations are absent, and hence that μ is purely real. In particular, we consider the locus of equilibria generated by equation for $s^{\mathbf{e}} = 14$, see Figure 6A. The (real) roots, μ, of Equation 62 for this case are shown in Figure 12. (For convenience the corresponding values of $G(s_{\mathbf{t}})$, from Figure 6A are shown.) For $s_{\mathbf{t}} > 22.5$ there is just one negative root of equation, indicating that the single equilibrium is stable,

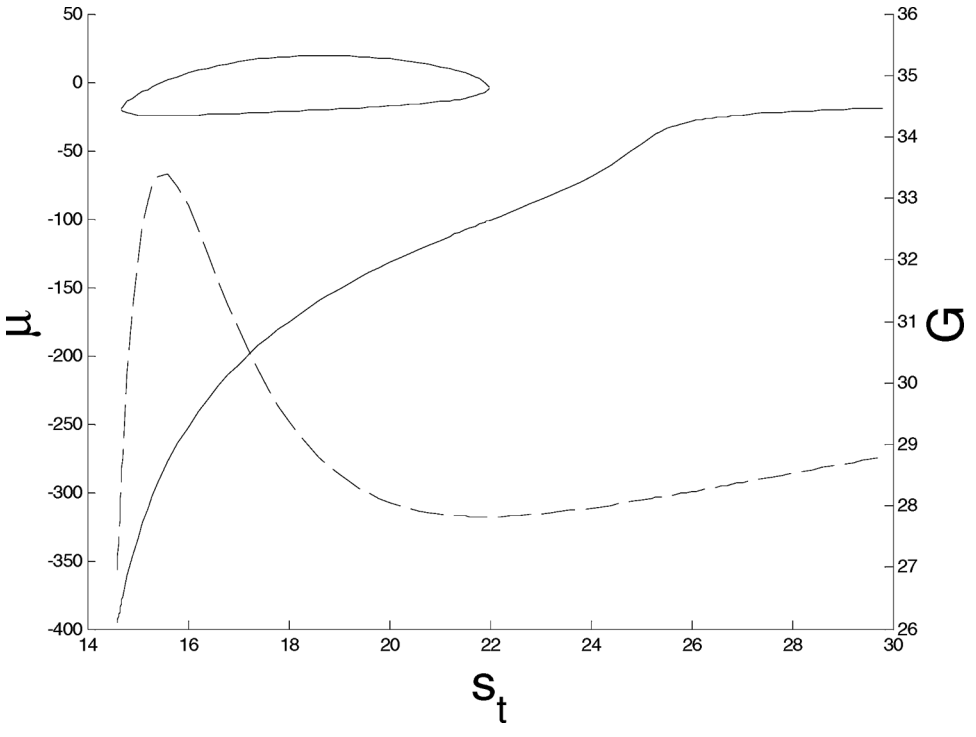

Figure 12. Locus of real solutions, μ, of Equation 62, for $t_d = 8$ msec and $s^e = 14$. The corresponding values of gain, G, from Figure 6A are shown as a dashed curve, with abscissa at right.

and the firing rate follows the curve given in Figure 4. For $14.5 < s_t < 22.5$ there are three real roots. For most of this range, one of the roots is positive implying instability. Thus, for this range there are two stable equilibria corresponding to a given value of G *and* $s^e = 14$. One of these fires at a substantially higher firing rate than shown in Figure 4. Figure 12 also indicates the possibility of three stable equilibria in small sub-regions at the right and left limits of the triple state interval. Two of these fire at much higher firing rates than shown in Figure 4.

On the basis of limited numerical explorations we have found that the higher firing rate equilibria (smaller values of $|\mu|$) in Figure 12 have relatively small basins of attraction. Thus, small, but finite, perturbations of these equilibria are unstable and drive such solutions to the low firing rate equilibrium. In this sense there is a resemblance to the cases discussed earlier.

Stochastic jumps

We can go beyond the model under study and consider how a stochastic range of sizes of synaptic response affects the firing properties of a population of neurons (see Appendix 1). This was first investigated by Knight (1972), and more recently by Fourcaud and Brunel (2002) using a Fokker-Planck formulation of integrate-and-fire dynamics. (See also Brunel & Latham (2003), for a similar treatment of the quadratic integrate-and-fire model.) The effect of this stochasticity is to introduce *diffusivity*, a stabilizing effect. For example, its inclusion raises the $t_d = 0$ stability boundary in Figure 9A.

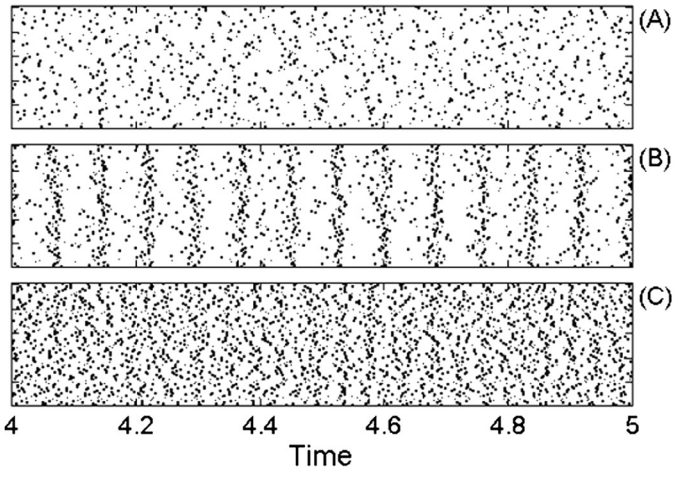

Figure 13. Raster plots of 100 neurons (out of a population of 1000) for $t_d = 3$ msec at the three gains: (A) $G = 15$; (B) $G = 20$; (C) $G = 25$. The three noisy curves in Figure 8C depict the firing rates of the full population.

Additional computations

To further illuminate and support our investigations we performed several relatively large scale calculations. First, we comment on some direct simulations that parallel the results displayed in Figure 9.

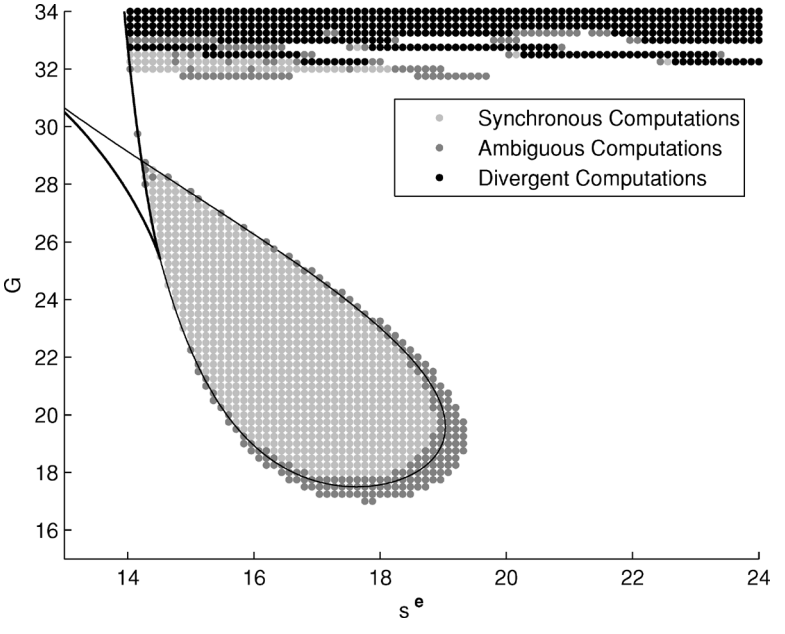

Figure 14. Extensive assay of ($s^{\mathbf{e}}$, G)-plane obtained by integrating Equation 7. White indicates stable asynchronous behavior. The cusp, heavy line, corresponds to that shown in Figure 6B. The teardrop curve, thin line, is the map of the $t_d = 3$ msec theoretical curve shown in Figure 10, for the stability boundary.

We carried out a direct simulation on a population network of 1000 neurons at three gains $G = 15, 20, 25$, and for $s^{\mathbf{e}} = 18$ and $t_d = 3$ msec. The result of these direct simulations are shown in the three raster plots of 100 neurons, each shown in Figure 13. The first and third panels confirm the asynchronous behavior predicted in Figure 9, and the middle plot confirms the synchronous behavior shown for $G = 20$. In addition the firing rates, shown as color coded (noisy) traces in Figure 9C, shows nice agreement with the smooth behavior from the population model of the same figure.

For further verification of our analysis, we undertook a broad assay of the behavior of solutions of the time dependent population Equation 15, over the $(s^{\mathbf{e}}, G)$-plane. In Figure 14, we show the result of this, again for $t_d = 3$ msec. All unshaded areas indicate regions where a synchronous activity was found. Light gray regions indicate synchronous behavior. Dark gray regions are *ambiguous*, i.e., the classifier used by the production algorithm to assay the $(s^{\mathbf{e}}, G)$-plane, was not able to make a determination in the allotted calculation time for these points. The *tear-drop* curve, which is the map of the theoretical $t_d = 3$ msec stability boundary, runs cleanly through the ambiguous region.

The black region at the top of the figure indicates divergence. To see the origin of this we observe that from Equation 15,

$$s_{\mathbf{t}}(t) = \frac{s^{\mathbf{e}}}{1 - G\int_{1-h}^{1} \rho(v,t)dv}. \tag{68}$$

Therefore, for $G \approx 1/h$ and larger, this current and hence the solution, will diverge in a finite time. (For example, for G large imagine initial data so that $\int_{1-h}^{1} \rho(v,t)dv \approx 0$ during the initial transient.) This divergence, a consequence of our deliberately simplified model would disappear if a dead time is included in the model.

Conclusions

We have seen that an assembly of coupled oscillators is capable of a wide range of behaviors. It should be noted that the *oscillators*, leaky integrate-and-fire neurons, themselves have no natural *rhythm*. Their time scale, the interspike interval is determined by the net current that they experience. Therefore, the natural rhythm of the population depends not only on the external input but also on the conditions of the network itself. At relatively low connectivity, G, each neuron can run with near clocklike precision, largely independent of its neighbors, which run in a similar, but uncorrelated state. The net result is a time stationary asynchronous population of neurons. Their probability distribution of states, i.e., membrane potentials, depends on s/γ, the ratio of net arrival current to leakage. Even when leakage dominates the current, firing can still occur. This effect is further leveraged by the presence of connectivity.

For increasing connectivity, or gain, a critical state is reached, when neurons can induce their neighbors to fire at nearly the *same* time. When this happens, the entire population attempts to march together, asynchrony is lost, and the population adopts the rhythm of the individual neuron. As gain is further increased, the firing rate of the population becomes extremely scalloped with extreme amplitudes. At a critical value of gain there is divergence in finite time, and a solution no longer exists.

This unrealistic limiting case can be attributed to any one of a number of properties which have not been incorporated into our model. For example, a neuron has a dead time (when a neuron *recoups* its resources) before it can fire again, also called the refractory period. If the dead time is denoted by τ_d, then $1/\tau_d$ puts a cap on the firing rate of a neuron. (A nominal value is $\tau_d \approx 2\ ms$.) Other features that can be incorporated into the model are the time of

transmission of spikes, and the duration of synaptic events. We have lumped such features together into a single quantity, t_d, the delay time.

Introduction of delay time had a profound effect on the range of behavior. Even the slightest delay destroys the possibility of synchrony in extensive regions of parameter space, replacing it with asynchrony. For realistic values of t_d, we found that synchrony occurs, but with a rhythm different from the mean firing rate. Moreover, delay discourages neurons from marching in lockstep, and more modest amplitudes are seen in the oscillating firing rates. At higher gains, time delay can replace synchrony by asynchrony. Finally, time delays only within some range of values permit synchrony . For the nominal case treated here, only asynchronous activity occurs for $t_d > 7.38$ msec, and in this case the intriguing possibility of multistates appeared. Thus, if synchrony is indeed relevant to the workings of neural tissue, it requires a narrow range of time delays.

Acknowledgments

The authors are grateful to Bruce W. Knight for his insightful observations during the course of this research. The authors are also grateful to two anonymous referees for valuable suggestions and to the Editor-in-Chief for his professional handling of the review process. This work was supported by Defense Advanced Research Planning Agency Grant MDA972-01-1-0028 and National Institute of Mental Health Grant 5R01MH50166.

This paper and related literature can be found at http://camelot.mssm.edu/

Appendix 1: Stochastic jumps

For the case of stochastic jumps in response to neuronal impulses the counter-part to Equation 5 is given by Omurtag et al. (2000a)

$$\frac{\partial \rho}{\partial \tau} = -\frac{\partial}{\partial v}\left\{ -\gamma v\rho + \sigma(t)\int_0^v \tau(v-v')\rho(v')dv' \right\}. \tag{1.1}$$

Here τ is the cumulative probability

$$\tau(h) = \int_h^1 p(h')dh' \tag{1.2}$$

for the probability density function, $p(h)$, of jump size h. The analysis of Equation 1.1 follows that given in the main text. For a given impulse rate σ_t, we obtain the equilibrium solution,

$$U = U(v, \sigma_{\mathbf{t}}) \tag{1.3}$$

which satisfies

$$\frac{\partial}{\partial v}\left\{ -\gamma vU + \sigma_{\mathbf{t}}\int_0^v \tau(v-v')U(v')dv' \right\} = 0. \tag{1.4}$$

The equilibrium impulse rate is given by

$$r_0 = \sigma_{\mathbf{t}}\int_0^1 \tau(1-v')U(v')dv' = \sigma_{\mathbf{t}}k. \tag{1.5}$$

To follow the development in Heuristic Considerations we define

$$L(\sigma_{\mathbf{t}})u = \frac{\partial}{\partial v}\left\{\gamma v u + \sigma_{\mathbf{t}} \int_0^v \tau(v - v')u(v')dv'\right\}, \tag{1.6}$$

$$\Phi(v) = \sigma_{\mathbf{t}} \int_0^v \tau(v - v')U(v', \sigma_{\mathbf{t}})dv' \tag{1.7}$$

$$(H, u) = \int_0^1 \tau(1 - v')u(v')dv' \tag{1.8}$$

from which follows that stability analysis leads to

$$\mu u = Lu + \Phi(v)\frac{G}{1 - kG}(H, u). \tag{1.9}$$

It is clear that Equation 1.9 can be treated by the same methods as those presented in earlier sections.

Appendix 2: Time delay

In real tissue, synaptic arrivals lag due to synaptic and signaling delays among other causes. To explore the affect of these, we lump the lags into a single time. t_d. Thus, the synaptic arrival rate $\sigma(t)$ is now given by

$$\sigma(t) = \sigma^{\mathbf{e}}(t) + Gr(t - t_d) = \sigma^{\mathbf{e}} + GT_d r. \tag{2.1}$$

Here, T_d represents the lag operator $T_d f(t) = f(t - t_d)$. The firing rate Equation 11, now becomes

$$r = (\sigma^{\mathbf{e}} + Gr(t - t_d))k(t), \tag{2.2}$$

or solving for r

$$r(t) = (1 - kGT_d)^{-1}\sigma^{\mathbf{e}}k. \tag{2.3}$$

If this is back substituted into Equation 2.1, we obtain

$$\sigma = \frac{1}{k}(1 - kGT_d)^{-1}(\sigma^{\mathbf{e}}k). \tag{2.4}$$

It follows that the kinetic equation now is

$$\frac{\partial \rho}{\partial t} = \gamma \frac{\partial}{\partial v}(v\rho) + \frac{1}{k}\{(1 - kGT_d)^{-1}(\sigma^{\mathbf{e}}k)\}(\rho(v - h, t) - \rho(v, t)) \tag{2.5}$$

which for $t_d \downarrow 0$ becomes Equation 15.

If we linearize about equilibrium 43, we obtain

$$\mu u = Lu + \Phi(v)\frac{Ge^{-\mu t_d}}{1 - kGe^{-\mu t_d}}(H, u) \tag{2.6}$$

for the determination of the stability parameter, μ. Note, if $t_d = 0$, Equation 2.6 reduces to 49. The dispersion relation for μ is now given by

$$1 = \frac{Ge^{-\mu t_d}}{1 - kGe^{-\mu t_d}} \sum_l \frac{(H, \phi_l)(\widehat{\phi}_l, \Phi)}{\mu - \lambda_l} \tag{2.7}$$

and the solution for u by

$$u = \frac{Ge^{-\mu t_d}}{1 - kGe^{-\mu t_d}} \sum_l \frac{(\widehat{\phi}_l, \Phi)}{\mu - \lambda_l} \phi_l. \tag{2.8}$$

The stability boundary is given by Equation 62 in analogy to 61.

References

Abbott L, van Vreeswijk C. 1993. Asynchronous states in networks of pulse-coupled oscillators. PRE 48:1483–1490.

Abeles M. 1991. Corticonics: neural circuits of the cerebral cortex. New York: Cambridge University Press.

Amit D, Brunel N. 1997. Model of global spontaneous activity and local structured activity during delay periods in the cerebral cortex. Cerebral Cortex 7:237–252.

Arnold V. 1965. Small denominators I: On the mapping of a circle into itself. Tran Am Math Soc, Ser 2, 46:213–284.

Arnold V. 1986. Catastrophe Theory. Berlin: Springer-Verlag.

Brunel N, Hakim V. 1999. Fast global oscillations in networks of integrate-and-fire neurons with low firing rates. Neural Comp 11:1621–1671.

Brunel N, Latham P. 2003. Firing rate of the noisy quadratic integrate-and-fire neuron. Neural Comp 15:2281–2306.

Cai D, Tao L, Shelley M, McLaughlin D. 2004. An effective kinetic representation of fluctuation-driven neuronal networks with application to simple and complex cells in visual cortex. PNAS 101:7757–7762.

Castelo-Branco M, Neuenschwander S, Singer W. 1998. Synchronization of visual responses between the cortex, lateral geniculate nucleus, and retina in the anesthetized cat. J Neurosci 18:6395–6410.

Casti A, Omurtag A, Sornborger A, Kaplan E, Knight B, Victor J, Sirovich L. 2002. A population study of integrate-and-fire-or-burst neurons. Neural Comp 14:957–986.

Cobb S, Buhl E, Halasy K, Paulsen O, Somogyi P. 1995. Synchronization of neural activity in hippocampus by individual GABAergic interneurons. Nature 378:75–78.

Courant R. 1936. Differential and Integral Calculus: Volume II. New York: Wiley-Interscience; Wiley Classics Library.

de Kamps M. 2003. A simple and stable numerical solution for the population density equation. Neural Comp 15:2129–2146.

Fourcaud N, Brunel N. 2002. Dynamics of the firing probability of noisy integrate-and-fire neurons. Neural Comp 14:2057–2110.

Friedman B. 1990. Principles and Techniques of Applied Mathematics. New York: Dover Publications.

Fusi S, Mattia M. 1999. Collective behavior of networks with linear (VLSI) integrate-and-fire neurons. Neural Comp 11:633–652.

Gardiner C. 1983. Handbook of stochastic methods. Berlin: Springer-Verlag.

Gerstner W. 1995. Time structure of the activity in neural network models. PRE 51:738–758.

Gerstner W. 2000. Population dynamics of spiking neurons: fast transients, asynchronous states and locking. Neural Comp 12:43–89.

Ghose G, Freeman R. 1997. Intracortical connections are not required for oscillators activity in the visual cortex. Visual Neuroscience 14:963–979.

Guckenheimer J, Holmes P. 1983. Nonlinear oscillations, dynamical systems and bifurcations of vector fields, volume 42 of Applied Mathematical Sciences. New York: Springer-Verlag.

Haskell E, Nykamp D, Tranchina D. 2001. Population density methods for large-scale modeling of neuronal networks with realistic synaptic kinetics: cutting the dimension down to size. Network: Comput Neural Syst 12:141–174.

Holden, A. 1976. Models of the stochastic activity of neurons. Springer Lecture Notes in Biomathematics. New York: Springer-Verlag.

Knight B. 1972. The relationship between the firing rate of a single neuron and the level of activity in a population of neurons: Experimental evidence for resonant enhancement in the population response. J Gen Physiol 59:767–778.

Knight B. 2000. Dynamics of encoding in neuron populations: some general mathematical features. Neural Comp 12:473–518.

Knight B, Manin D, Sirovich L. 1996. Dynamical models of interacting neuron populations. In: Symposium on Robotics and Cybernetics: Computational Engineering in Systems Applications (Gerf, E.C. ed) Cite Scientifique, Lille, France.

Knight B, Omurtag A, Sirovich L. 2000. Dynamics of neuronal populations: Analytic solution of step-transient response compared to direct simulation. Neural Comp 12:1045–1055.

Kuramoto Y. 1991. Collective synchronization of pulse-coupled oscillators and excitable units. Physica D 50:15–30.

Kuramoto Y. 2003. Chemical Oscillations, Waves and Turbulence. New York:Dover Publications.

Lytton W, Sejnowski T. 1991. Simulations of cortical pyramidal neurons synchronized by inhibitory interneurons. J Neurophysiol 66:1059–1079.

Mattia M, Del Giudice P. 2002. Population dynamics of interacting spiking neurons. Phys Rev E 66:051917.

Milner P. 1974. A model for visual shape recognition. Psychol Rev 81:521–535.

Mirollo E, Strogatz S. 1990. Synchronization of pulse-coupled biological oscillators. SIAM J Appl Math 50:1645–1662.

Naundorf B, Geisel T, Wolf F. 2005. Action potential onset dynamics and the response speed of neuronal populations. J. Computational Neuroscience 18:297–309.

Niebur E, Schuster H, Kammen D, Koch C. 1991. Oscillator-phase coupling for different two-dimensional network connectivities. Physical Review A 44:6895–6904.

Nykamp D, Tranchina D. 2000. A population density approach that facilitates large-scale modeling of neural networks: analysis and an application to orientation tuning. J Comp Neurosci 8:19–50.

Omurtag A, Knight B, Sirovich L. 2000a. On the simulation of large populations of neurons. J. Comp. Neurosci. 8:51–63.

Omurtag A, Kaplan E, Knight B, Sirovich L. 2000b. A population approach to cortical dynamics with an application to orientation tuning. Network 11:247–260.

Peskin C. 1975. Mathematical Aspects of Heart Physiology. Courant Institute of Mathematical Sciences, New York University, New York.

Ratliff F, Knight B, Graham N. 1969. On tuning and amplification by lateral inhibition. PNAS 62:733–740.

Ritz R, Sejnowski T. 1997. Synchronous oscillatory activity in sensory systems: new vistas on mechanisms. Current Opinion in Neurobiol 7:536–546.

Schuster H, Wagner P. 1990. A model for neuronal oscillations in the visual cortex. Biol Cybern 64:77–82.

Sillito A, Jones H, Gerstein G, West D. 1994. Feature-linked synchronization of thalamic relay cell firing induced by feedback from the visual cortex. Nature 369:479–482.

Singer W, Gray C. 1995. Visual feature integration and the temporal correlation hypothesis. Annual Review of Neuroscience 18:555–586.

Sirovich L. 2003. Dynamics of neuronal populations: eigenfunction theory; some solvable cases. Network: Comput Neural Syst 14:249–272.

Sirovich L, Knight B, Omurtag A. 2000. Dynamics of neuronal populations: The equilibrium solution. SIAM J Appl Math 60:2009–2028.

Stein R. 1965. A theoretical analysis of neuronal variability. Biophys J 5:173–194.

Strogatz S. 2000. Nonlinear Dynamics and Chaos. Colorado: Westview Press.

Strogatz S. 2003. Sync: The emerging science of spontaneous order. New York: Hyperion Press.

Treves A. 1993. Mean-field analysis of neuronal spike dynamics. Network: Comput Neural Syst 4:259–284.

Tsodyks M, Mitkov I, Sompolinsky H. 1993. Pattern of synchrony in inhomogeneous networks of oscillators with pulse interactions. PRL 71:1280–1283.

Tuckwell H, Cope D. 1980. Accuracy of neuronal interspike times calculated from a diffusion approximation. J. Theoretical Biology 83:377–387.

Von der Malsberg C. 1994. Models of Neural Networks II, chapter The Correlation Theory of Brain Function, pp 95–119. Berlin: Springer-Verlag.

Wilbur W, Rinzel J. 1982. An analysis of Stein's model for stochastic neuronal excitation. Biol Cybern 45:107–114.